Linking function to global and local dynamics in an elevator-type transporter

Didar Ciftci[a,b,1], Chloe Martens[c,1,2], Vishnu G. Ghani[a], Scott C. Blanchard[d], Argyris Politis[c], Gerard H. M. Huysmans[a,3], and Olga Boudker[a,b,e,3]

[a]Department of Physiology and Biophysics, Weill Cornell Medicine, New York, NY 10065; [b]Tri-Institutional Training Program in Chemical Biology, New York, NY 10065; [c]Department of Chemistry, King's College London, London SE1 1DB, United Kingdom; [d]Department of Structural Biology, St. Jude Children's Research Hospital, Memphis, TN 38105; and [e]Howard Hughes Medical Institute, Weill Cornell Medicine, New York, NY 10065

Edited by Robert H. Edwards, University of California, San Francisco, CA, and approved September 29, 2021 (received for review December 15, 2020)

Transporters cycle through large structural changes to translocate molecules across biological membranes. The temporal relationships between these changes and function, and the molecular properties setting their rates, determine transport efficiency—yet remain mostly unknown. Using single-molecule fluorescence microscopy, we compare the timing of conformational transitions and substrate uptake in the elevator-type transporter Glt_{Ph}. We show that the elevator-like movements of the substrate-loaded transport domain across membranes and substrate release are kinetically heterogeneous, with rates varying by orders of magnitude between individual molecules. Mutations increasing the frequency of elevator transitions and reducing substrate affinity diminish transport rate heterogeneities and boost transport efficiency. Hydrogen deuterium exchange coupled to mass spectrometry reveals destabilization of secondary structure around the substrate-binding site, suggesting that increased local dynamics leads to faster rates of global conformational changes and confers gain-of-function properties that set transport rates.

single-molecule FRET | hydrogen deuterium exchange mass spectrometry | conformational dynamics | rate-limiting step | glutamate transporter

Transporters are integral membrane proteins that move solutes across lipid bilayers. They undergo concerted conformational changes, allowing alternate exposure of their substrate-binding sites to external and internal solutions (1). In each of these so-called outward- and inward-facing states (OFS and IFS, respectively), further isomerizations accompany substrate binding and release. Transport efficiency depends on the rates of these rearrangements, but linking function and structural dynamics has presented methodological challenges. Single-molecule Forster resonance energy transfer (smFRET)-based total internal reflection fluorescence (TIRF) microscopy (2–4) has been used to monitor the dynamics of the OFS to IFS transitions (5–8) and single-transporter activity (9) in the elevator-type transporter Glt_{Ph} and other transporters (10–18). Hydrogen–deuterium exchange followed by mass spectrometry (HDX-MS) has been used to pinpoint local changes in structural dynamics in diverse biological systems (19–21). Here, we combine these approaches to link changes in local protein dynamics to the larger-scale conformational transitions and substrate transport in wild-type (WT) and gain-of-function mutants of Glt_{Ph}.

Glt_{Ph} is an extensively studied archaeal aspartate transporter that is homologous to human excitatory amino acid transporters (EAATs). Structures of Glt_{Ph} (7, 22–30), and archaeal and mammalian homologs (31–37), show that the transporters assemble into homotrimers via scaffold domains. Each protomer features a mobile transport domain that binds L-Aspartate (L-Asp) and three Na^+ ions (22, 23, 28, 31, 38) and symports the solutes by an elevator mechanism, moving ~15 Å across the membrane from an OFS to an IFS (6, 8, 23, 24, 39). During the elevator transitions, two structurally symmetric helical hairpins (HPs) 1 and 2 form the cores of the domain interfaces in the OFS and IFS, respectively (*SI Appendix*, Fig. S1*A*) (23, 24, 40). Despite symmetry, they do not have the same function. HP1 is mostly rigid, while HP2 is a conformationally plastic "master regulator" of the transporter, gating substrate in the OFS and IFS and contributing to setting the elevator transition rates (5, 23, 24, 27, 29, 36, 41–47).

In this study, we use three previously characterized mutants of Glt_{Ph} to pinpoint the rate-limiting steps of the transport cycle and probe the protein dynamic properties that correlate with increased transport rates. A K290A mutation at the base of HP1 disrupts a salt bridge with the scaffold domain in the OFS and dramatically increases the elevator dynamics (5, 6). A triple-mutant Y204L/A345V/V366A displays a more modest increase in elevator dynamics and substantially diminished L-Asp affinity (5). Finally, a Y204L/K290A/A345V/V366A mutant combines these substitutions and their effects (5). We compared our previously obtained smFRET data on the elevator dynamics of the WT transporter and the mutants (5) to single-transporter uptake measurements. For WT Glt_{Ph}, these dynamics and transport measurements established transporter subpopulations that move (5, 6) and work (9) with rates differing by orders of magnitude, with slow transporters dominating the ensemble. We now show that only mutations that both reduce the population of the

Significance

Structural snapshots of membrane transporters show that they cycle through several conformational states to bring substrates across the membrane. The rates of these molecular motions determine the activity of the transporters. In this work, we directly compare real-time single-molecule measurements of conformational changes and substrate transport rates in the model glutamate transporter homologue, Glt_{Ph}. We couple these experiments with hydrogen–deuterium exchange mass spectrometry measurements of local protein flexibility to directly link local and global conformational dynamics with function.

Author contributions: D.C., C.M., S.C.B., A.P., G.H.M.H., and O.B. designed research; D.C., C.M., V.G.G., and G.H.M.H. performed research; S.C.B. and A.P. contributed new reagents/analytic tools; D.C., C.M., V.G.G., G.H.M.H., and O.B. analyzed data; and D.C., C.M., V.G.G., S.C.B., G.H.M.H., and O.B. wrote the paper.

Competing interest statement: S.C.B. holds an equity interest in Lumidyne Technologies.

This article is a PNAS Direct Submission.

[1]D.C. and C.M. contributed equally to this work.

[2]Present address: Centre for Structural Biology and Bioinformatics, Universite Libre de Bruxelles, 1050 Bruxelles, Belgium.

[3]To whom correspondence may be addressed. Email: gerard.huysmans@gmail.com or olb2003@med.cornell.edu.

This article contains supporting information online at http://www.pnas.org/lookup/suppl/doi:10.1073/pnas.2025520118/-/DCSupplemental.

Published December 3, 2021.

slow-moving transporters and weaken substrate affinity, such as Y204L/A345V/V366A, reduce the population of the slow-working transporters and confer overall gain-of-function properties. The slow-working population comprises transporters with rare elevator transitions or slow substrate release. We then used HDX-MS to explore how the Y204L/A345V/V366A mutant differed from the WT protein. We found that the mutations decreased the stability of the secondary structure around the substrate-binding site, suggesting that the increased local dynamics underlie reduced kinetic heterogeneity within the mutant transporter ensemble.

Results

Substrate Translocation Can Limit the Transport Rate. We previously developed two TIRF-based single-molecule assays that follow elevator dynamics and transport activity of Glt_{Ph} under near-identical conditions (5–7, 9) (Fig. 1). Glt_{Ph} variants were labeled with a mixture of the donor and acceptor dyes and polyethylene glycol 11 (PEG_{11})-biotin before reconstitution into liposomes for smFRET conformational dynamics experiments. In contrast, Glt_{Ph} variants were labeled only with PEG_{11}-biotin and reconstituted into liposomes with encapsulated L-Asp–binding protein ccPEB1A-Y198F labeled with donor and acceptor dyes for single-transporter activity assays (9). We then assayed Glt_{Ph} dynamics and activity in the presence of ionic gradients required for concentrative transport. The internal liposome buffers were devoid of Na^+ ions or L-Asp, while the external buffers contained 200 mM Na^+ and a saturating L-Asp concentration. In the transport assays, the time between the substrate application and the first observed increase of FRET efficiency (E_{FRET}) of the encapsulated fluorescently labeled ccPEB1a-Y198F marks

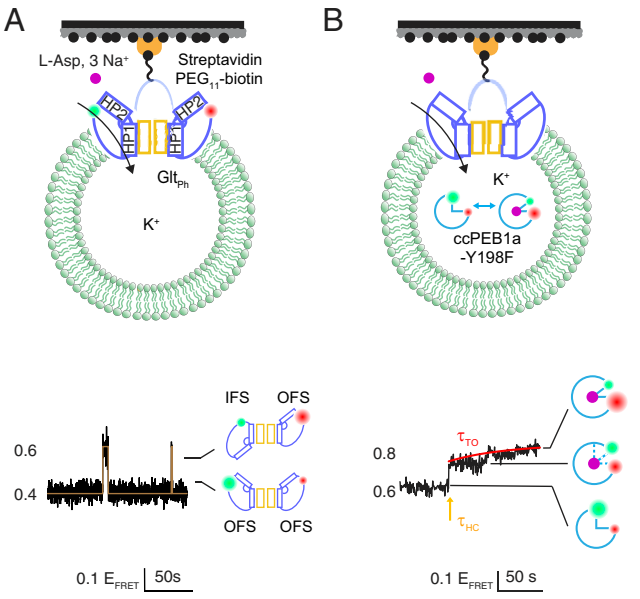

Fig. 1. Single-molecule assays of Glt_{Ph} elevator dynamics and transport. (*A*) The experimental setup for the time-resolved smFRET measurements of Glt_{Ph} elevator transitions (*Top*). An example of a dynamics trajectory acquired in the presence of an internal buffer containing 200 mM KCl and an external buffer containing 200 mM NaCl and 100 μM L-Asp (*Bottom*). The brown line shows the idealization obtained in Spartan. (*B*) The experimental setup for smFRET-based single-transporter uptake assay (*Top*). An example of a transport trajectory recorded in the presence of an internal buffer containing 200 mM KCl and an external buffer containing 200 mM NaCl and 1 μM L-Asp, corresponding to near-saturating conditions (*Bottom*). The yellow arrow marks the entry of the first L-Asp molecule. The red line is the fit to the time-dependent binding equation.

the completion of the first half-cycle, τ_{HC}, which includes L-Asp binding, translocation, and release into the liposome (Fig. 1*B*). Fitting the subsequent gradual E_{FRET} increase due to further rounds of L-Asp transport to a time-dependent mass action binding equation yields a mean turnover time, τ_{TO} (Fig. 1*B* and *Materials and Methods*) (9).

We compared previously measured elevator dynamics (5) with single-transporter activities of WT Glt_{Ph}, taken from ref. 9, and of gain-of-function mutants, measured in this study (Fig. 2 and *SI Appendix*, Figs. S1 and S2). Mean transport rates of WT Glt_{Ph} and the Y204L/A345V/V366A mutant (~0.01 and 0.08 s^{-1}) agreed well with their mean transition frequencies (~0.01 and 0.12 s^{-1}) (Fig. 2 *A* and *B*). Similar to WT transporters (9), the transport rates of individual Y204L/A345V/V366A molecules deviated substantially from the mean, ranging from less than 0.01 s^{-1} to over 1 s^{-1} (Fig. 2 *A*, *Top* and *B*, *Top* and *SI Appendix*, Figs. S3 and S4). However, the mutant transporters showed a higher fraction of faster uptake, with 26 ± 6% (compared to 8 ± 2% of the WT) completing the first half-cycle within 5 s (the fast component in *SI Appendix*, Table S1). About half of Y204L/A345V/V366A molecules (55 ± 13% compared to 72 ± 7% for the WT) did not complete a single transport half-cycle before the fluorescently labeled ccPEB1a-Y198F photobleached (mean τ_{PB} = ~60 s). For convenience, we term this subpopulation as "nonresponding." Notably, however, most of the nonresponding transporters do complete their transport cycle within 30 min following substrate addition, showing that, while slow, they are active (9). The uptake results are in excellent agreement with the elevator dynamics measurements, which showed that 48 ± 7% and 80 ± 2% of the substrate bound Y204L/A345V/V366A mutant and WT Glt_{Ph} transporters, respectively, did not make excursions into the IFS before the fluorophores photobleached (Fig. 2 *A*, *Middle* and *B*, *Middle*).

All transporters that completed multiple rounds of transport (37 ± 14% of the mutant and 15 ± 6% of the WT) showed similar τ_{HC} and τ_{TO}, yielding two-dimensional (2D) population histograms elongated along the diagonal (Fig. 2 *A*, *Top* and *B*, *Top*). Thus, subpopulations of transporters appear to work at constant but different rates over several turnovers. Similar τ_{HC} and τ_{TO} values further indicate that the half-cycle—substrate binding, translocation, and release—is the rate-limiting part of the complete cycle. Consistently, the distributions of the OFS lifetimes covered the same ranges as τ_{HC} and τ_{TO} values for both variants, with the majority of the molecules populating the E_{FRET} state corresponding to the OFS. IFS lifetime distributions and their means were comparatively short (Fig. 2 *A*, *Middle* and *B*, *Middle*) (5). Taken together, these uptake and dynamics data indicate that substrate translocation represents the rate-limiting step in these transporters, while the return of the empty transporter back into the OFS is comparatively fast (Fig. 2 *A*, *Bottom* and *B*, *Bottom*).

In line with our earlier studies (5, 9), the transporters comprise subpopulations that, following substrate binding in the OFS, translocate into the IFS with different rates, which are maintained over several turnovers. The interconversion between the apparent "dynamic modes" rarely occurs on the timescale of our observations, so that only 5 to 20% of the single-molecule dynamics traces display shifts between modes (5, 9). The measured distributions of τ_{HC}, τ_{TO}, and τ_{OFS} shifted to shorter times in Y204L/A345V/V366A mutant, suggesting that these mutations increased the population of faster-working, more dynamic transporters, similar to previously characterized R276S/M395R gain-of-function mutations (7, 9).

Substrate Release Can Limit the Transport Rate. The variants containing K290A mutations showed slower transport activity than elevator dynamics (Fig. 2 *C* and *D* and *SI Appendix*, Figs. S1

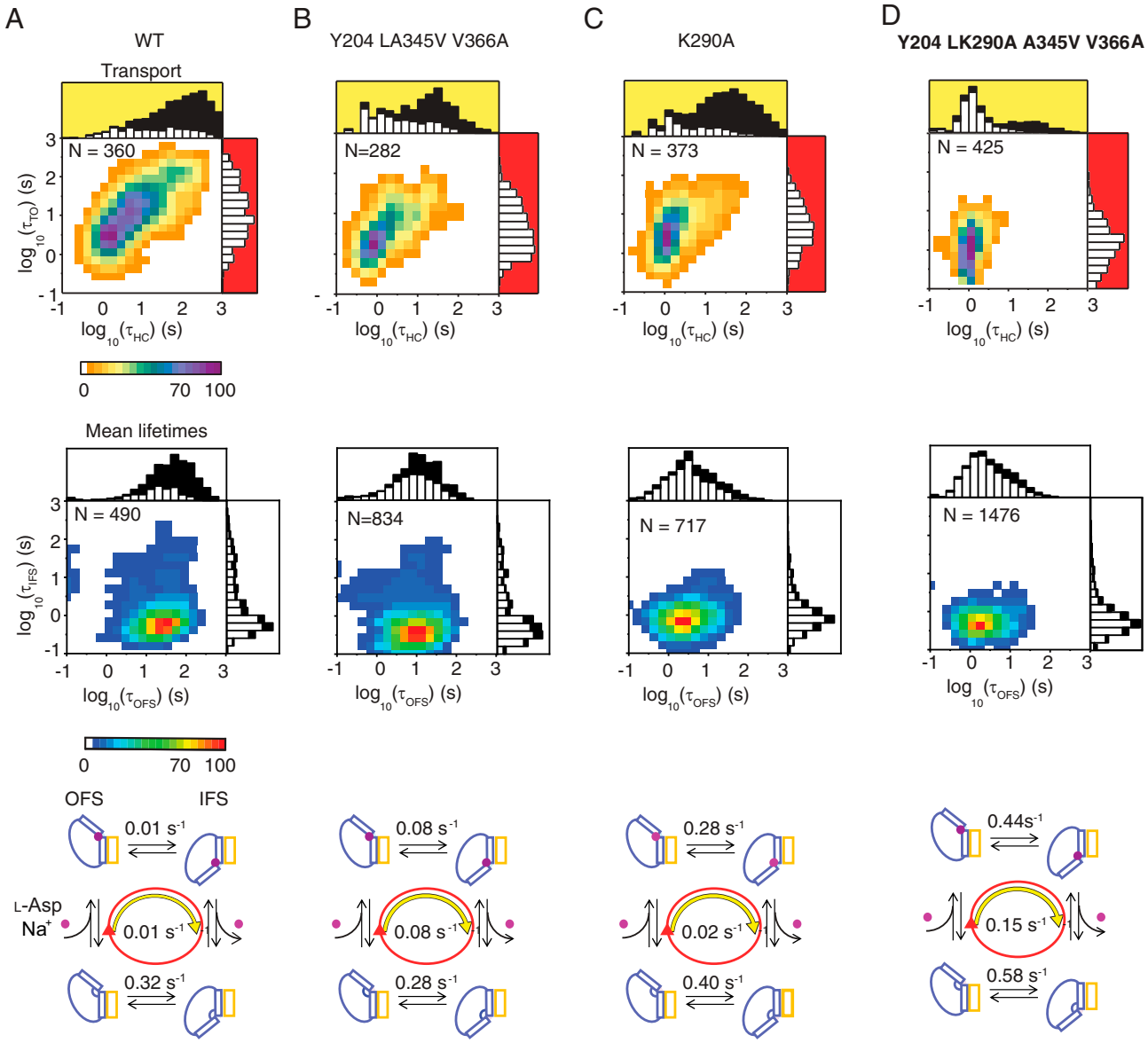

Fig. 2. Substrate uptake and elevator dynamics of Glt_{Ph} WT (*A*) and mutants (*B–D*). (*Top*) The 2D histograms of τ_{HC} and τ_{TO} pairs measured for individual transporters. 1D histograms of τ_{HC} (top, shaded yellow) and τ_{TO} (right, shaded red) are shown as white bars adjacent to the 2D histograms. Black bars are the lifetimes (τ_{PB}) of labeled ccPEB1a-Y198F molecules that photobleached before a transport event (nonresponding). Scale bar is shown at the bottom. (*Middle*) The 2D population histograms of mean paired OFS and IFS lifetimes of individual transporter molecules (τ_{OFS} and τ_{IFS}). The 1D histograms of τ_{OFS} (top) and τ_{IFS} (right) are shown as white bars adjacent to the 2D histograms. Black bars are the lifetimes of nonresponding, labeled Glt_{Ph} molecules that photobleached before showing transitions (τ_{PB}). The scale bar is at the bottom. Data are from ref. 5. (*Bottom*) Schematic representations of the transport cycles of the transporters. Mean elevator transition frequencies are above the arrows. The mean transport rates are in the center of each diagram. The transition frequencies and rates, and corresponding errors, are shown in *SI Appendix*, Table S1.

and S2 and Table S1). In particular, K290A Glt_{Ph} showed ~30-fold increased mean elevator transition frequency and only a twofold increase in mean transport rate compared to the WT transporter. Like WT Glt_{Ph}, the majority of the K290A transporters (76 ± 8%) did not complete a single transport half-cycle, displaying similarly broad distributions of τ_{HC} and τ_{TO} (Fig. 2 *C*, *Top* and *SI Appendix*, Figs. S3 and S4). Thus, although the K290A mutation is more effective in increasing the elevator dynamics through enriching the fast dynamic mode compared to the Y204L/A345V/V366A mutations, this increase does not translate into higher transport rates.

Therefore, substrate translocation is not rate limiting in the K290A transporters. Since K290A IFS lifetimes are still short (Fig. 2 *C*, *Middle*), either binding or release of Na^+ ions and L-Asp must be slow in this mutant. We measured the kinetics of Na^+ and L-Asp binding using the voltage-sensitive amphipathic dye RH421 (28, 48–50) upon the addition of 200 mM NaCl to the protein samples in the presence of L-Asp, that is, under conditions matching single-molecule transport assays. Single exponential kinetics described fluorescence changes well, yielding rate constants of 0.92 ± 0.12 s^{-1} and 0.58 ± 0.04 s^{-1} for the WT and K290A transporters, respectively(*SI Appendix*, Fig. S5 *A* and *B*). We observed similar rates at lower Na^+ concentrations (10 mM NaCl, 100 μM L-Asp) (*SI Appendix*, Fig. S5 *C* and *D*). These comparatively fast binding rates are consistent with earlier reports on WT Glt_{Ph} (6, 48, 51–53). Previous studies suggested that HP2 might undergo slow conformational changes following rapid Na^+ binding (46), although others have

challenged these conclusions (53). We compared single-molecule transport kinetics with and without preequilibrating vesicles in 200 mM Na^+ and observed no significant differences (*SI Appendix*, Fig. S6). Together, these results suggest that Na^+ and L-Asp binding and associated conformational changes of the transporter are not rate limiting in WT and K290A variant.

Thus, the release rates from the IFS span at least two orders of magnitude and limit the transport rate in most K290A Glt_{Ph} molecules. To verify that the L-Asp dissociation from the IFS can be rate limiting in the K290A transport cycle, we measured the release rates for the Glt_{Ph} variants directly. We introduced our gain-of-function mutations within the Glt_{Ph} background containing the following mutations: P11W/K55C/C221A/A364C (48). We cross-linked the mutants in the IFS using Hg^{2+} (24) and used tryptophan fluorescence to follow substrate dissociation. Glt_{Ph} does not contain native tryptophan, and P11W fluorescence has been shown to report on substrate release kinetics without affecting binding (48). Proteins were rapidly diluted into buffers with 1 mM Na^+ ions in the absence of L-Asp, leading to substrate release and the tryptophan fluorescence decay (*SI Appendix*, Fig. S7). The WT and K290A mutant showed similar slow substrate dissociation kinetics, with fitted rates of 0.062 ± 0.001 and 0.0129 ± 0.0003 s^{-1}(*SI Appendix*, Fig. S7). These ensemble measurements do not allow detailed kinetic analysis. Nevertheless, we note that biexponential functions fitted the fluorescence decay data better than single exponentials, consistent with heterogeneous release rates (*SI Appendix*, Fig. S7).

The Y204L/A345V/V366A mutant, like K290A, diminishes the population of the transporters with slow dynamics, albeit not as efficiently. However, unlike the K290A mutant, it shows less heterogeneous transport rates that parallel elevator dynamics and a diminished fraction of nonresponding transporters (Fig. 2*B*). Thus, the Y204L/A345V/V366A mutant must have a reduced or absent population of slow-releasing transporters. Indeed, we measured a several-fold faster mean L-Asp release rate from the IFS of the Y204L/A345V/V366A mutant compared to the WT and K290A transporters (*SI Appendix*, Fig. S7), consistent with the 20-fold lower substrate affinity (5). Combining the K290A and Y204L/A345V/V366A mutations should lead to synergistic increase of the elevator dynamics and the L-Asp release. In the single-molecule transport assay, Y204L/K290A/A345V/V366A Glt_{Ph} showed a mean transport rate of 0.15 ± 0.06 s^{-1}, faster than either the Y204L/A345V/V366A or K290A mutants (Fig. 2*D* and *SI Appendix*, Fig. S1*B*), with most transporters showing transport ($62 \pm 6\%$) and elevator transitions ($73 \pm 6\%$) during the observation window and having rapid substrate release (*SI Appendix*, Fig. S7). The distributions of the OFS and IFS lifetimes and τ_{HC} and τ_{TO} times were very similar, with markedly reduced heterogeneity.

Y204L/A345V/V366A Glt_{Ph} Exhibits Increased Flexibility around the Substrate-Binding Site. Our mutations suggest that only simultaneous increases of elevator dynamics and L-Asp release rates, such as in the Y204L/A345V/V366A mutant, accelerate Glt_{Ph} function. Surprisingly, however, the crystal structure of Y204L/A345V/V366A Glt_{Ph} in the OFS was very similar to that of the WT transporter (5). To understand the effect of the Y204L/A345V/V366A mutations, we turned to HDX-MS to probe the structural flexibility and local dynamics of the mutant. HDX of labile backbone amide protons depends on H-bond stability and accessibility to bulk deuterium (19, 54). Changes in the HDX rate reflect solvent exposure and stability of the local secondary structure or other interactions involving backbone amides. We proteolyzed Glt_{Ph} variants for fragment separation MS analysis after isotopic labeling at various time points and subsequent quenching to locate regions with variable exchange rates. Sequence coverage of the detected peptides ranged from 77 to 83% across individual repeats (*SI Appendix*, Fig. S8 and *Materials and Methods*).

We first compared HDX in the Y204L/A345V/V366A mutant and WT Glt_{Ph} under apo conditions. We expressed the differences in deuterium uptake as changes in the relative fractional uptake (ΔRFU), which is positive when regions take up more deuterium in the mutant relative to WT Glt_{Ph} or negative when they are better protected from uptake. There was little HDX in the scaffold domain of both Glt_{Ph} variants (Fig. 3*A* and *SI Appendix*, Fig. S8 *A* and *C*), showing that its structural rigidity and stability remain unaffected by the mutations. In contrast, we observed significant HDX in the transport domain that was higher in Y204L/A345V/V366A Glt_{Ph}, with positive ΔRFU values varying between 25% and 45% (Fig. 3*B* and *SI Appendix*, Fig. S9). Peptides encompassing parts of HP1, HP2, and the transmembrane (TM) helices 7 and 8 exchanged significantly faster in the mutant compared to WT over multiple biological repeats (Fig. 3 *B–D* and *SI Appendix*, Fig. S9). These regions surround the substrate-binding site and also form the interfaces with the scaffold domain. In contrast, lipid-facing TM3 and TM6 in the transport domain showed low HDX in both proteins.

When we carried out the HDX measurements in the presence of saturating L-Asp and Na^+ concentrations, we observed exchange in the same regions as in the apo proteins, but HPs 1 and 2 and TM7 and TM8 showed less exchange in both WT and Y204L/A345V/V366A Glt_{Ph} (*SI Appendix*, Figs. S8, S10, and S11). However, the mutant still showed higher exchange compared to the WT transporter, resulting in decreased but positive ΔRFUs for most peptides (*SI Appendix*, Fig. S9 *C* and *D*). Only TM8 became fully protected in the mutant(*SI Appendix*, Figs. S8 and S9 *C* and *D*), suggesting the structural rearrangements upon substrate binding particularly stabilize this α-helix.

Overall, the HDX data suggest that Y204L/A345V/V366A mutations lead to increased protein flexibility around the substrate-binding site, particularly in the apo protein (Fig. 3). In the WT transporter, HP2 occludes the substrate binding both when bound to L-Asp and in the apo-form (23, 29, 31, 33, 42, 55). Therefore, HP2 likely protects proximal protein regions from HDX. Consistently, there are comparatively small differences in the extent of HDX with and without the substrate in WT Glt_{Ph} (*SI Appendix*, Fig. S10 *A* and *B*). However, these differences are more pronounced in the Y204L/A345V/V366A mutant (*SI Appendix*, Figs. S10 *C* and *D* and S11), suggesting that HP2 has a higher propensity to open, increasing dynamics and water access to regions around the entire substrate-binding site.

Discussion

We have established a direct correlation between conformational dynamics and transport in the glutamate transporter homolog Glt_{Ph} by comparing single-transporter activity and elevator dynamics. Using Glt_{Ph} mutants that only boost the conformational dynamics or also diminish substrate affinity, we deduce that the transport cycle has two kinetically heterogeneous steps, substrate translocation from the OFS to IFS, and release from the IFS, and both can become rate limiting. Remarkably, mutations in HP2 affect rates of both processes, highlighting the critical role that this region plays in setting the functional properties of the transporter. In contrast, the return of the transport domain into the OFS and the coupled binding of Na^+ ions and L-Asp are comparatively fast.

The transporter subpopulations with different rates of elevator transitions and substrate release are unlikely to be due to heterogeneous biochemical processing, such as proteolysis or posttranslational modifications. First, we produce Glt_{Ph} in

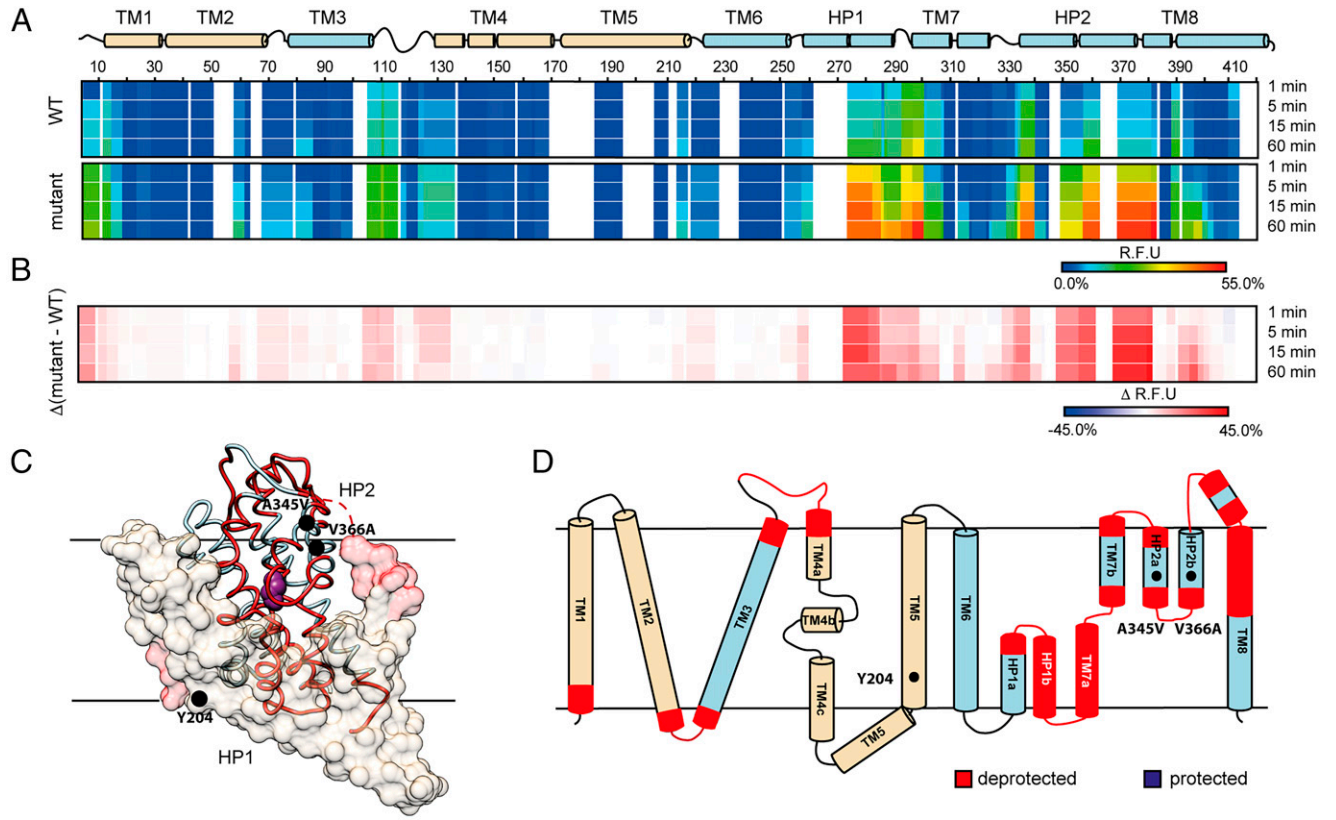

Fig. 3. Effect of Y204L/A345V/V366A mutations on apo Glt_{Ph} local dynamics measured by HDX-MS. (*A*) Heat maps representing the RFU of WT (*Top*) and Y204L/A345V/V366A mutant (*Bottom*) apo-Glt_{Ph} (in buffer containing 200 mM KCl). Shown is a representative experiment from three biological replicates (*SI Appendix*, Fig. S8). The secondary structure elements of Glt_{Ph} are shown on top. The scaffold domain is colored wheat, and the transport domain is light blue. The RFU of deuterium at each incubation time (1, 5, 15, and 60 min) is displayed according to the rainbow color code shown. Uncolored regions indicate areas with no peptide coverage. (*B*) ΔRFU, comparing Glt_{Ph} mutant minus the WT. Red and blue indicate relative deprotection and protection, respectively. (*C* and *D*) Peptides, consistently showing significant (99% CI) deprotection upon mutation, mapped on the 3D structure (*C*; Protein Data Bank accession code 2NWX), and the topological 2D map (*D*). In *C*, the scaffold domain is shown as a transparent surface to facilitate visualization of the transport domain, depicted as ribbons. L-asp is shown as spheres to indicate the location of the binding site.

Escherichia coli, which lacks posttranslational modification machinery (56). Second, point mutations can eliminate both dynamics and transport rate heterogeneities. Instead, our observations suggest that there are conformational substates that persist over multiple transport turnovers. "Slow" substates encounter high energy barriers during transport domain translocation from the OFS to IFS and/or during substrate gating in the IFS (Fig. 4). "Fast" transporters encounter reduced barriers during both processes. Structural studies have shown that both the elevator transitions and substrate gating in the IFS involve remodeling of the interface between the transport and scaffold domains and, in particular, conformational changes of HP2 interacting with the scaffold (7, 22–24, 29, 47). Furthermore, our earlier experiments suggested that the principal energy barrier of the OFS-to-IFS transition involves forming a stable interface between HP2 and the scaffold in the IFS (5). It is likely that A345V and V366A mutations in HP2, located on the interface between the hairpin and the transport domain core, affect the local protein packing. Together, these considerations implicate HP2 as a structural determinant of both energy barriers.

How do the Y204L/A345V/V366A mutations reduce the energy barriers of the elevator dynamics and L-Asp release? HDX-MS revealed that the mutations decrease the structural rigidity of the protein regions around the substrate-binding site, including HP2. Thus, we suggest that, in Y204L/A345V/V366A Glt_{Ph}, rapid local fluctuations of HP2 favor substrate release and facilitate access to subpopulations with faster elevator dynamics. Coupling of fast nanosecond-to-microsecond local structural fluctuations to large-scale concerted movements on the millisecond-to-second timescale, underlying catalytic activity, has been demonstrated in enzymes (57, 58). Furthermore, a comparison of enzymes from thermophilic and mesophilic organisms showed that increased activity at lower temperatures correlates with increased protein flexibility (59). Glt_{Ph} originates from a hyperthermophilic archaeon and shows much lower activity at room temperature than its mesophilic counterparts (23, 38, 60–63). Therefore, it is, perhaps, not unexpected that the protein demonstrates rigidity at ambient temperatures in HDX-MS experiments, and mutations leading to increased protein flexibility also lead to increased activity, akin to natural thermal adaptations.

HP2 mutations, located over 10 Å away from the binding site, might weaken L-Asp affinity by increasing the conformational entropic penalty of binding. NMR spectroscopy was previously employed to experimentally correlate the losses of conformational entropy to decreased binding affinity in protein/protein and protein/DNA interactions (64, 65). While HDX-MS does not provide equivalent information, it is notable that the Y204L/A345V/V366A mutant shows a greater loss of flexibility upon substrate binding compared to the WT transporter, which would be consistent with the larger loss of conformational entropy.

Our results show that subtle packing mutations, such as in the Y204L/A345V/V366A Glt_{Ph}, or single mutations breaking polar interactions, such as K290A, can modulate the energy barriers of the transport cycle and alter which step is rate

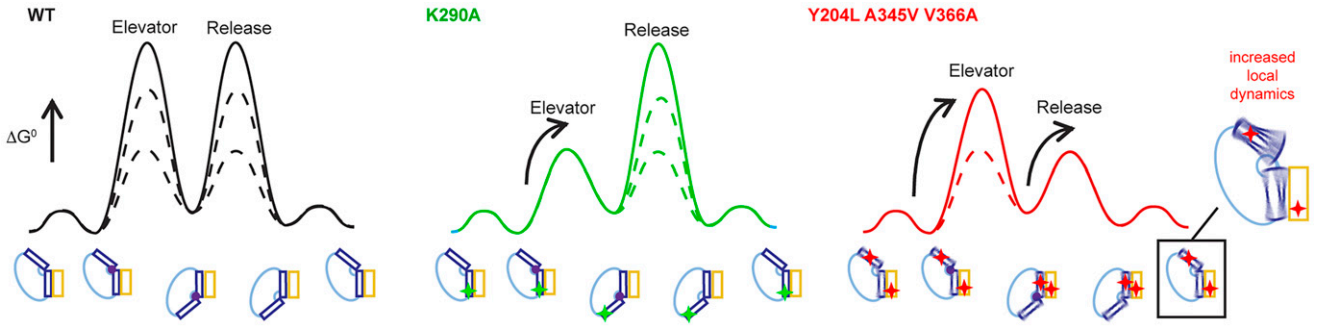

Fig. 4. Simplified energy diagram of the transport cycle and its modulation by mutations. Cartoons of the low-energy states are shown below the diagrams. Stars indicate the locations of the mutations. For illustration purposes, energy differences between all states are considered small compared to the energy difference with the rate-limiting transition states. Dashed lines represent heterogeneity in the isomerization of L-Asp/Na^+–loaded Glt_{Ph} and the L-Asp release rate.

limiting. Thus, it is likely that homologous glutamate transporters have different rate-limiting steps. For example, the rate-limiting step in mammalian glutamate transporters is the return of the potassium-bound transport domain to the OFS (66–68). Intriguingly, stabilizing a closed conformation of HP2 in EAAT1 and EAAT2 renders it potassium independent (47), suggesting that HP2 has a similarly critical role in defining the energy landscape of these transporters. Finally, while observed in many cases (69–75), it remains unknown how widespread kinetic heterogeneities are. Further studies will reveal their potential existence and physiological relevance in mammalian transporters and whether these heterogeneities can be modulated by cellular factors or sequence variations.

Materials and Methods

Glt_{Ph} Purification and Labeling for Single-Transport Experiments. All Glt_{Ph} variants containing a single engineered cysteine (N378C/C321A), seven engineered histidines to optimize expression, and a hexahistidine tag for affinity purification were produced, purified, and labeled as described previously (6). Briefly, Glt_{Ph} was produced in *E. coli* DH10b(DE3) cells, deficient in Lon and OmpT proteases, grown in lysogeny broth (LB) medium supplemented with 100 μg/mL ampicillin and induced with 20 mM L-arabinose for 3 h at 37 °C. Cells were disrupted, and membranes were isolated by 1 h of centrifugation at 100,000 × *g* at 4 °C. Membranes were homogenized in 50 mM Hepes, pH 7.4, 200 mM NaCl, 1 mM L-Asp, and 0.1 or 1 mM Tris (2-carboxyethyl) phosphine (TCEP) and solubilized with 40 mM n-dodecyl β-D-maltopyranoside (DDM) for 1 h at 4 °C. Insoluble material was removed by centrifugation (1 h at 100,000 × *g* and 4 °C). Glt_{Ph} was purified using nickel nitrilotriacetic acid (Ni-NTA) agarose (Qiagen) in the same buffer with 1 mM DDM and eluted with 250 mM imidazole. Following thrombin cleavage of the His_6-tag, Glt_{Ph} was further purified by size exclusion chromatography (SEC) using a Superdex 200 column (GE Healthcare) in buffer containing 20 mM Hepes, pH 7.4, 200 mM NaCl, 0.1 mM L-Asp, 1 mM DDM. For transport experiments, Glt_{Ph} variants were labeled with maleimide-activated biotin-PEG_{11} (EZ-link, Thermo Fisher Scientific) and *N*-ethyl maleimide (NEM) at a molar ratio of 1:2:4 of protein:biotin-PEG_{11}:NEM. Excess reagents were removed by SEC. Protein samples were concentrated to 3 mg/mL to 4 mg/mL using 100-kDa cutoff concentrators (EMD Millipore) and reconstituted immediately into liposomes.

PEB1a Purification and Labeling. The PEB1a protein with C18S, N73C, K149C, and Y198F mutations (ccPEB1a-Y198F) was expressed and purified, as described previously (9). Briefly, cells were grown in LB medium supplemented with 100 μg/mL ampicillin and induced with 1 mM isopropyl β-D-1-thiogalactopyranoside for 3 h at 37 °C followed by 16 h at 18 °C. Cells were disrupted via osmotic shock and centrifuged for 30 min at ∼3,600 × *g* at 4 °C to pellet the debris. The protein was purified by Ni-NTA chromatography (Qiagen) in buffer containing 50 mM Hepes/Tris, pH 7.4, 200 mM NaCl, 1 mM TCEP, eluting with 250 mM imidazole. Protein was further purified by SEC in 50 mM Hepes/Tris, pH 7.4, 200 mM NaCl and immediately labeled with LD555P and LD655 at a molar ratio of 1:1:1.5 of protein:LD555P:LD655 for 1 h at 25 °C. Excess reagents were removed by SEC in 50 mM Hepes/Tris, pH 7.4, 200 mM KCl. Protein samples were concentrated to 3 μM to 4 μM using 10-kDa cutoff concentrators (EMD Millipore).

Glt_{Ph} Reconstitution into Liposomes and ccPEB1a-Y198F Encapsulation. Labeled Glt_{Ph} variants were reconstituted into liposomes as previously described (6). Briefly, liposomes were prepared from 3:1 (wt/wt) mixture of *E. coli* polar lipid extract (Avanti Polar Lipids, Inc.) and egg phosphatidylcholine in a buffer containing 50 mM Hepes/Tris, pH 7.4, and 200 mM KCl and extruded through 400-nm filters (Whatman Nuclepore) using a syringe extruder (Avanti Polar Lipids, Inc.). Liposomes were destabilized by the addition of Triton X-100 at 1:2 (wt/wt) detergent-to-lipid ratio, and Glt_{Ph} was added at 1:1,000 protein-to-lipid ratio. The protein/lipid mixture was incubated at 25 °C for 30 min. Detergent was removed by four to six rounds of incubation with Biobeads (Bio-Rad) at 100 mg/mL. For transport measurements, fluorescently labeled ccPEB1a-Y198F was encapsulated at a final concentration of 0.6 μM by two freeze–thaw cycles. To remove excess ccPEB1a-Y198F from the external solution, the proteoliposomes were centrifuged for 1 h at 66,125 × g at 4 °C. Resuspended proteoliposomes were concentrated to ∼25 mg/mL and extruded through 100-nm filters 11 times before imaging.

smFRET Transport Measurements and Data Analysis. Data for Glt_{Ph} dynamics were taken from ref. 5 and reanalyzed to obtain the characteristic OFS and IFS lifetimes of each molecule. OFS and IFS lifetimes were mathematically corrected for the missed transitions (76). Transport data for the WT transporter were taken from ref. 9. Single-molecule transport data for all mutants were collected and analyzed as described previously (9). Experiments were performed using a home-built prism-based TIRF microscope constructed around a Nikon Eclipse Ti inverted microscope body (77). The samples were illuminated with a 532-nm laser (LaserQuantum), LD555P, and LD655 fluorescence signals were separated using a T635lpxr dichroic filter (Chroma) mounted in a Multi-Cam apparatus (Cairn). A home-written acquisition software, kindly provided by the S.C.B. laboratory, and scientific complementary metal oxide semiconductor cameras (Hamamatsu) were used to acquire data. Microfluidic imaging chambers were either passivated with biotin-PEG as previously described (7) or with methoxy-PEG succinimidyl propionate (mPEG-SPA), MW 1000, (Laysan Bio, Inc.), and *N*-hydroxysuccinimide (NHS)-PEG4-Biotin (EZ-Link). Briefly, slides with drilled holes and coverslips were cleaned as previously described (78) and incubated with passivation reagents for 16 h. After incubation, they were rinsed thoroughly with distilled water and dried. Sample chambers were assembled by attaching the slide and the coverslip using 50-μm-thick double-sided tape as previously described (78). After assembly, the microfluidic chamber was incubated with 10 mM Tris/HCl, pH 7.4, 50 mM KCl supplemented with 0.8 μM streptavidin (Invitrogen) for 7 min and rinsed thoroughly. Proteoliposomes were immobilized via biotinylated transporters by incubating 5 μL to 7 μL of samples in the chamber for up to 1 min. Unbound vesicles were washed away with the internal buffer. Time-dependent fluorescence emission intensities were extracted and selected using SPARTAN software (77). FRET trajectories were calculated using the formula FRET = $I_{LD655}/(I_{LD555P} + I_{LD655})$, where I_{LD555p} and I_{LD655} are intensities of LD555P and LD655, respectively. Proteoliposome samples were tested for leakage in buffer containing 50 mM Hepes/Tris, pH7.4, and 200 mM KCl supplemented with 1 μM to 5 μM L-Asp (*SI Appendix*, Fig. S2). Transport was initiated by rapid exchange of the external buffer for 50 mM Hepes/Tris, pH7.4, 200 mM NaCl, and 1 μM to 5 μM L-Asp, approximately 3 s after the start of imaging. All buffers were supplemented with an oxygen scavenging system containing 2 mM protocatechuic acid and 50 nM protocatechuate-3,4-dioxygenase (79). Data were collected using 200-ms integration time at 20-mW laser power for the gain-of-function mutants and 400 ms and 40 mW for WT

Glt_{Ph}. Trajectories that lasted longer than 15 frames with a signal-to-noise ratio of at least eight and an initial E_{FRET} between 0.4 and 0.7 were selected to extract τ_{HC} and τ_{TO}. Further manual curation was performed to remove trajectories with an apparent lack of anticorrelation between fluorophore intensities and multiple donor or acceptor photobleaching events indicating unspecific labeling of the sensor or multiple sensors as described previously (9) (*SI Appendix*, Fig. S2). Removed trajectories usually correspond to 30 to 40% of the dataset. The shortest observed τ_{HC} in each dataset was used to approximate the substrate application time. We also supplemented L-Asp/NaCl buffers with 10 nM LD655 and used the increased background intensity to assess the time of buffer entry (*SI Appendix*, Fig. S2). The comparison shows that the shortest τ_{HC} agrees well with the apparent buffer entry times with a maximum shift of one to two frames (*SI Appendix*, Fig. S2). Cumulative frequency distributions of τ_{HC} were multiplied by the average responding molecule percentage for each mutant and were fitted to biexponential or triexponential association functions using Prism (Graphpad) to calculate $\%_{fast}$, $\%_{int}$, and $\%_{slow}$, the percentages of molecules transporting with fast, intermediate, and slow rates, k_{fast}, k_{int}, and k_{slow}, respectively (*SI Appendix*, Table S1). Mean transport rates per monomer (*SI Appendix*, Table S1), $k_{transport}$, were calculated as

$$k_{transport} = \frac{\%_{fast} * k_{fast} + \%_{int} * k_{int} + \%_{slow} * k_{slow})}{3}.$$

Histograms and population contour plots of τ_{HC} and τ_{TO} were prepared using Origin (Originlab Corporation). The τ_{HC} histograms were fitted to a transformed probability density function as described in ref. 80 based on the rate constants calculated from the cumulative frequency distributions (*SI Appendix*, Fig. S4).

$$PDF(x) = ln\ (10)\ * 10^{(x-x0)} * e^{10^{(x-x0)}},$$

where x is

$$x = log_{10}(\tau_{HC}).$$

RH421 Fluorescence Binding Kinetics Measurements. Glt_{Ph} variants were exchanged by SEC into a buffer containing 20 mM Hepes/Tris pH 7.4, 1 mM NaCl, 200 mM Choline-Cl, 1 mM DDM. Samples were diluted to a final concentration of 0.2 μM in buffer containing 20 mM Hepes/Tris pH 7.4, 200 mM KCl, 0.4 mM DDM, 200 nM RH421, and 1 mM TCEP in the presence or absence of various concentrations of L-Asp. RH421 was excited at 532 nm, and emission was measured at 628 nm. Samples were preincubated at 25 °C until the fluorescence signal plateaued. NaCl or L-Asp was added, and the fluorescence signal was recorded until equilibrium was reached. The signal was corrected for dilution, and the fluorescence decay curves, reflecting Na^+ or coupled Na^+ and L-Asp binding, were fitted to single exponential functions in Prism (Graphpad).

Fluorescence-Based L-Asp Release Measurements. Purified Glt_{Ph} variants harboring P11W/K55C/C321A/A364C mutations were exchanged into a buffer containing 20 mM Hepes/Tris pH7.4, 200 mM NaCl, 1 mM L-Asp, and 1 mM DDM using 100-kDa cutoff Amicon centrifugal filters to have the final concentration of TCEP below 0.1 μM. Proteins at concentration 0.5 mg/mL were immediately mixed with a 10-fold molar excess of $HgCl_2$ and incubated at room temperature for 15 min. Excess reagents were removed by SEC in a buffer containing 20 mM Hepes/Tris pH 7.4, 190 mM KCl, 10 mM NaCl, 0.3 mM L-Asp, and 1 mM DDM. Peak protein fractions were collected and concentrated to 1 mg/mL. For real-time fluorescence measurements of L-Asp release, samples were diluted 100-fold into a buffer containing 20 mM Hepes/Tris pH7.4, 190 mM KCl, 1 mM NaCl, 1 mM DDM. Tryptophan fluorescence was excited at 295 nm, and emission was measured at 350 nm with the following integration times: 0.4 or 1 s for WT and K290A and 0.2 s for Y204L/A345V/V366A and Y204L/K290A/A345V/V366A variants. After signal equilibration, saturating amounts of NaCl and L-Asp were added. The fluorescence signal was corrected for dilution and normalized by the signal increase observed after NaCl and L-Asp addition. The decay curves were fitted to a single or biexponential function in Prism (Graphpad). Approximately 10% reduction in protein fluorescence was observed upon dissociation. Release rates and SEs from three independent experiments are shown on *SI Appendix*, Fig. S7.

HDX-MS Data Collection and Analysis. HDX-MS experiments were done on a Synapt G2-Si coupled to nanoACQUITY ultra-performance liquid chromatography (UPLC) with HDX Automation technology (Waters Corporation). WT and Y204L A345V V366A Glt_{Ph} (without engineered cysteines) were purified as above and concentrated to ~30 μM. Five-microliter protein samples were incubated for 1 min, 5 min, 15 min, and 60 min in 95 μL of deuterium labeling buffer containing 20 mM Hepes, pD 8.5, 200 mM NaCl, 1mM L-Asp, 0.025% β-DDM for the bound conditions or 20 mM Hepes, pH 8.5, 200 mM KCl, 0.025% β-DDM for the apo conditions. The protein samples were then digested on Enzymate ethylene bridged hybrid (BEH) pepsin C18 column (Waters) at 20 °C. Peptides were trapped and desalted for 3 min on ACQUITY BEH C18 1.7-μm VANGUARD precolumn at a 200 μL/min flow rate using 0.1% formic acid in HPLC water pH 2.5. Peptides were then eluted to an ACQUITY UPLC BEH C18 1.7-μm analytical column with a linear gradient (8 to 40%) of 0.1% formic acid in acetonitrile at a flow rate of 40 μL/min. A cleaning run using a sawtooth gradient was performed between each sample run to reduce peptide carryover. Peptides were ionized through electrospray ionization (ESI) source in a positive ion mode using Synapt G2-Si mass spectrometer (Waters), with ion mobility separation (HD-MS^E). The unlabeled reference measurements were performed using 95 μL of 20 mM Hepes, pH8.5, 200 mM NaCl, 1mM L-Asp, 0.025% β-DDM for the bound references or 95 μL of 20 mM Hepes, pH8.5, 200 mM KCl, 0.025% β-DDM for the apo references. Between injections, the pepsin column was washed with 1.5 M Gu-HCl, 4% (vol/vol) MeOH, 0.8% (vol/vol) formic acid. Leucine Enkephalin was injected in the source in parallel for mass accuracy correction, and sodium iodide was used for the mass spectrometer calibration. $HDMS^E$ data were acquired using a 20- to 30-V trap collision energy ramp. All the isotope labeling time points were performed in triplicate, and the reference points were performed in quintuplicate. Acquired reference MS^E data were analyzed on PLGS (ProteinLynx Global Server 2.5.1, Waters) to determine the peptide map. All $HDMS^E$ data, including reference and deuterated samples, were then processed by DynamX v.3.0 (Waters) for deuterium uptake determination. Peptide filtration and analysis were performed as described before (81). Specifically, the amount of relative deuterium uptake for each peptide was determined using DynamX (v. 3.0) and is not corrected for back exchange. The RFU was calculated from $RFU_a = [Y_{a,t}/(MaxUptake_a \times D)]$, where Y is the deuterium uptake for peptide a at incubation time t, and D is the percentage of deuterium in the present in the sample after mixing the protein with the labeling solution. Statistical evaluation and filtering according to a 99% CI were performed using Deuteros software. All the peptides passing the filtering test were mapped on the 3D structure and topological map of the protein of interest. Woods plots were generated using the same software (82).

Data Availability. All data needed to evaluate the conclusions in the paper are included in the article and *SI Appendix*. Raw data for single molecule FRET trajectories can be found in GitHub, https://github.com/BoudkerLab/PNAS_data Uptake plots of the HDX-MS data can be accessed on Figshare (DOIs: 10.6084/m9.figshare.16825315; 10.6084/m9.figshare.16825306; 10.6084/m9.figshare.16825300)

ACKNOWLEDGMENTS. We thank Roger Altman for the preparation of smFRET chambers, Daniel S. Terry for providing access to the TIRF microscopy setup for single-molecule imaging, and William Eng for assistance with protein production. Funding was provided by The National Institute of Neurological Disorders and Stroke (NINDS) Grants R37NS085318 and R01NS111767 to O.B., American Heart Association (AHA) Fellowship 19PRE34380215 to D.C., and Grant 7R01GM098859 to S.C.B. This project has received funding from the European Union's Horizon 2020 research and innovation program under the Maire Sklodowska-Curie Grant Agreement MEMDYN 660083 (G.H.M.H.). A.P.'s work was supported by the Wellcome Trust Grant (109854/Z/15/Z) and the Leverhulme Trust Grant (RPG-2019-178). C.M. is a Research Fellow of the Fonds National de la Recherche Scientifique (FRS-FNRS, Belgium).

1. D. Drew, O. Boudker, Shared molecular mechanisms of membrane transporters. *Annu. Rev. Biochem.* **85**, 543–572 (2016).
2. E. Lerner *et al.*, Toward dynamic structural biology: Two decades of single-molecule Förster resonance energy transfer. *Science* **359**, eaan1133 (2018).
3. S. Weiss, Measuring conformational dynamics of biomolecules by single molecule fluorescence spectroscopy. *Nat. Struct. Biol.* **7**, 724–729 (2000).
4. C. Joo, H. Balci, Y. Ishitsuka, C. Buranachai, T. Ha, Advances in single-molecule fluorescence methods for molecular biology. *Annu. Rev. Biochem.* **77**, 51–76 (2008).
5. H. M. G. Huysmans, D. Ciftci, X. Wang, S. C. Blanchard, O. Boudker, The high-energy transition state of the glutamate transporter homologue GltPh. *EMBO J.* **40**, e105415 (2020).
6. N. Akyuz, R. B. Altman, S. C. Blanchard, O. Boudker, Transport dynamics in a glutamate transporter homologue. *Nature* **502**, 114–118 (2013).
7. N. Akyuz *et al.*, Transport domain unlocking sets the uptake rate of an aspartate transporter. *Nature* **518**, 68–73 (2015).
8. G. B. Erkens, I. Hänelt, J. M. Goudsmits, D. J. Slotboom, A. M. van Oijen, Unsynchronised subunit motion in single trimeric sodium-coupled aspartate transporters. *Nature* **502**, 119–123 (2013).

9. D. Ciftci *et al.*, Single-molecule transport kinetics of a glutamate transporter homolog shows static disorder. *Sci Adv.* **6**, eaaz1949 (2020).
10. M. Yang *et al.*, Single-molecule probing of the conformational homogeneity of the ABC transporter BtuCD. *Nat. Chem. Biol.* **14**, 715–722 (2018).
11. L. Wang *et al.*, Characterization of the kinetic cycle of an ABC transporter by single-molecule and cryo-EM analyses. *eLife* **9**, e56451 (2020).
12. J. M. H. Goudsmits, D. J. Slotboom, A. M. van Oijen, Single-molecule visualization of conformational changes and substrate transport in the vitamin B_{12} ABC importer BtuCD-F. *Nat. Commun.* **8**, 1652 (2017).
13. C. C. Su *et al.*, Structures and transport dynamics of a *Campylobacter jejuni* multidrug efflux pump. *Nat. Commun.* **8**, 171 (2017).
14. D. S. Terry *et al.*, A partially-open inward-facing intermediate conformation of LeuT is associated with Na^+ release and substrate transport. *Nat. Commun.* **9**, 230 (2018).
15. M. Dyla *et al.*, Dynamics of P-type ATPase transport revealed by single-molecule FRET. *Nature* **551**, 346–351 (2017).
16. Y. Zhao *et al.*, Substrate-modulated gating dynamics in a Na+-coupled neurotransmitter transporter homologue. *Nature* **474**, 109–113 (2011).
17. Y. Zhao *et al.*, Single-molecule dynamics of gating in a neurotransmitter transporter homologue. *Nature* **465**, 188–193 (2010).
18. G. A. Fitzgerald *et al.*, Quantifying secondary transport at single-molecule resolution. *Nature* **575**, 528–534 (2019).
19. E. Trabjerg, Z. E. Nazari, K. D. Rand, Conformational analysis of complex protein states by hydrogen/deuterium exchange mass spectrometry (HDX-MS): Challenges and emerging solutions. *TrAC Trend Anal. Chem.* **106**, 125–138 (2018).
20. L. Konermann, J. Pan, Y. H. Liu, Hydrogen exchange mass spectrometry for studying protein structure and dynamics. *Chem. Soc. Rev.* **40**, 1224–1234 (2011).
21. C. Martens, A. Politis, A glimpse into the molecular mechanism of integral membrane proteins through hydrogen-deuterium exchange mass spectrometry. *Protein Sci.* **29**, 1285–1301 (2020).
22. D. Yernool, O. Boudker, Y. Jin, E. Gouaux, Structure of a glutamate transporter homologue from *Pyrococcus horikoshii*. *Nature* **431**, 811–818 (2004).
23. O. Boudker, R. M. Ryan, D. Yernool, K. Shimamoto, E. Gouaux, Coupling substrate and ion binding to extracellular gate of a sodium-dependent aspartate transporter. *Nature* **445**, 387–393 (2007).
24. N. Reyes, C. Ginter, O. Boudker, Transport mechanism of a bacterial homologue of glutamate transporters. *Nature* **462**, 880–885 (2009).
25. G. Verdon, O. Boudker, Crystal structure of an asymmetric trimer of a bacterial glutamate transporter homolog. *Nat. Struct. Mol. Biol.* **19**, 355–357 (2012).
26. A. J. Scopelliti, J. Font, R. J. Vandenberg, O. Boudker, R. M. Ryan, Structural characterisation reveals insights into substrate recognition by the glutamine transporter ASCT2/SLC1A5. *Nat. Commun.* **9**, 38 (2018).
27. X. Wang, O. Boudker, Large domain movements through the lipid bilayer mediate substrate release and inhibition of glutamate transporters. *eLife* **9**, e58417 (2020).
28. N. Reyes, S. Oh, O. Boudker, Binding thermodynamics of a glutamate transporter homolog. *Nat. Struct. Mol. Biol.* **20**, 634–640 (2013).
29. G. Verdon, S. Oh, R. N. Serio, O. Boudker, Coupled ion binding and structural transitions along the transport cycle of glutamate transporters. *eLife* **3**, e02283 (2014).
30. I. Chen *et al*., Glutamate transporters have a chloride channel with two hydrophobic gates. *Nature* **591**, 327–331 (2021).
31. A. Guskov, S. Jensen, I. Faustino, S. J. Marrink, D. J. Slotboom, Coupled binding mechanism of three sodium ions and aspartate in the glutamate transporter homologue Glt_{Tk}. *Nat. Commun.* **7**, 13420 (2016).
32. S. Jensen, A. Guskov, S. Rempel, I. Hänelt, D. J. Slotboom, Crystal structure of a substrate-free aspartate transporter. *Nat. Struct. Mol. Biol.* **20**, 1224–1226 (2013).
33. V. Arkhipova, A. Guskov, D. J. Slotboom, Structural ensemble of a glutamate transporter homologue in lipid nanodisc environment. *Nat. Commun.* **11**, 998 (2020).
34. J. C. Canul-Tec *et al.*, Structure and allosteric inhibition of excitatory amino acid transporter 1. *Nature* **544**, 446–451 (2017).
35. A. A. Garaeva *et al.*, Cryo-EM structure of the human neutral amino acid transporter ASCT2. *Nat. Struct. Mol. Biol.* **25**, 515–521 (2018).
36. A. A. Garaeva, A. Guskov, D. J. Slotboom, C. Paulino, A one-gate elevator mechanism for the human neutral amino acid transporter ASCT2. *Nat. Commun.* **10**, 3427 (2019).
37. X. Yu *et al.*, Cryo-EM structures of the human glutamine transporter SLC1A5 (ASCT2) in the outward-facing conformation. *eLife* **8**, e48120 (2019).
38. R. M. Ryan, E. L. Compton, J. A. Mindell, Functional characterization of a Na+-dependent aspartate transporter from *Pyrococcus horikoshii*. *J. Biol. Chem.* **284**, 17540–17548 (2009).
39. Y. Ruan *et al.*, Direct visualization of glutamate transporter elevator mechanism by high-speed AFM. *Proc. Natl. Acad. Sci. U.S.A.* **114**, 1584–1588 (2017).
40. T. J. Crisman, S. Qu, B. I. Kanner, L. R. Forrest, Inward-facing conformation of glutamate transporters as revealed by their inverted-topology structural repeats. *Proc. Natl. Acad. Sci. U.S.A.* **106**, 20752–20757 (2009).
41. I. H. Shrivastava, J. Jiang, S. G. Amara, I. Bahar, Time-resolved mechanism of extracellular gate opening and substrate binding in a glutamate transporter. *J. Biol. Chem.* **283**, 28680–28690 (2008).
42. P. J. Focke, P. Moenne-Loccoz, H. P. Larsson, Opposite movement of the external gate of a glutamate transporter homolog upon binding cotransported sodium compared with substrate. *J. Neurosci.* **31**, 6255–6262 (2011).
43. Z. Huang, E. Tajkhorshid, Dynamics of the extracellular gate and ion-substrate coupling in the glutamate transporter. *Biophys. J.* **95**, 2292–2300 (2008).
44. E. Zomot, I. Bahar, Intracellular gating in an inward-facing state of aspartate transporter Glt(Ph) is regulated by the movements of the helical hairpin HP2. *J. Biol. Chem.* **288**, 8231–8237 (2013).
45. J. DeChancie, I. H. Shrivastava, I. Bahar, The mechanism of substrate release by the aspartate transporter GltPh: Insights from simulations. *Mol. Biosyst.* **7**, 832–842 (2011).
46. E. A. Riederer, F. I. Valiyaveetil, Investigation of the allosteric coupling mechanism in a glutamate transporter homolog via unnatural amino acid mutagenesis. *Proc. Natl. Acad. Sci. U.S.A.* **116**, 15939–15946 (2019).
47. D. Kortzak *et al.*, Allosteric gate modulation confers K^+ coupling in glutamate transporters. *EMBO J.* **38**, e101468 (2019).
48. S. Oh, O. Boudker, Kinetic mechanism of coupled binding in sodium-aspartate symporter GltPh. *eLife* **7**, e37291 (2018).
49. M. Pedersen *et al.*, Detection of charge movements in ion pumps by a family of styryl dyes. *J. Membr. Biol.* **185**, 221–236 (2002).
50. M. Habeck, E. Cirri, A. Katz, S. J. Karlish, H. J. Apell, Investigation of electrogenic partial reactions in detergent-solubilized Na,K-ATPase. *Biochemistry* **48**, 9147–9155 (2009).
51. I. Hänelt, S. Jensen, D. Wunnicke, D. J. Slotboom, Low affinity and slow Na+ binding precedes high affinity aspartate binding in the secondary-active transporter GltPh. *J. Biol. Chem.* **290**, 15962–15972 (2015).
52. D. Ewers, T. Becher, J. P. Machtens, I. Weyand, C. Fahlke, Induced fit substrate binding to an archeal glutamate transporter homologue. *Proc. Natl. Acad. Sci. U.S.A.* **110**, 12486–12491 (2013).
53. C. Alleva *et al.*, Na^+-dependent gate dynamics and electrostatic attraction ensure substrate coupling in glutamate transporters. *Sci. Adv.* **6**, eaba9854 (2020).
54. J. R. Engen, Analysis of protein conformation and dynamics by hydrogen/deuterium exchange MS. *Anal. Chem.* **81**, 7870–7875 (2009).
55. E. A. Riederer *et al.*, A facile approach for the in vitro assembly of multimeric membrane transport proteins. *eLife* **7**, e36478 (2018).
56. A. Hochkoeppler, Expanding the landscape of recombinant protein production in Escherichia coli. *Biotechnol. Lett.* **35**, 1971–1981 (2013).
57. K. A. Henzler-Wildman *et al.*, A hierarchy of timescales in protein dynamics is linked to enzyme catalysis. *Nature* **450**, 913–916 (2007).
58. S. Mittal, Y. Cai, M. N. Nalam, D. N. Bolon, C. A. Schiffer, Hydrophobic core flexibility modulates enzyme activity in HIV-1 protease. *J. Am. Chem. Soc.* **134**, 4163–4168 (2012).
59. P. Závodszky, J. Kardos, G. A. Svingor, G. A. Petsko, Adjustment of conformational flexibility is a key event in the thermal adaptation of proteins. *Proc. Natl. Acad. Sci. U.S.A.* **95**, 7406–7411 (1998).
60. I. Gaillard, D. J. Slotboom, J. Knol, J. S. Lolkema, W. N. Konings, Purification and reconstitution of the glutamate carrier GltT of the thermophilic bacterium *Bacillus stearothermophilus*. *Biochemistry* **35**, 6150–6156 (1996).
61. M. Rahman *et al.*, Characterisation of the DAACS family *Escherichia coli* glutamate/aspartate-proton symporter GltP using computational, chemical, biochemical and biophysical methods. *J. Membr. Biol.* **250**, 145–162 (2017).
62. B. Tolner, T. Ubbink-Kok, B. Poolman, W. N. Konings, Characterization of the proton/glutamate symport protein of *Bacillus subtilis* and its functional expression in *Escherichia coli*. *J. Bacteriol.* **177**, 2863–2869 (1995).
63. D. Yernool, O. Boudker, E. Folta-Stogniew, E. Gouaux, Trimeric subunit stoichiometry of the glutamate transporters from Bacillus caldotenax and *Bacillus stearothermophilus*. *Biochemistry* **42**, 12981–12988 (2003).
64. S. R. Tzeng, C. G. Kalodimos, Protein activity regulation by conformational entropy. *Nature* **488**, 236–240 (2012).
65. K. K. Frederick, M. S. Marlow, K. G. Valentine, A. J. Wand, Conformational entropy in molecular recognition by proteins. *Nature* **448**, 325–329 (2007).
66. C. Grewer, N. Watzke, M. Wiessner, T. Rauen, Glutamate translocation of the neuronal glutamate transporter EAAC1 occurs within milliseconds. *Proc. Natl. Acad. Sci. U.S.A.* **97**, 9706–9711 (2000).
67. D. E. Bergles, A. V. Tzingounis, C. E. Jahr, Comparison of coupled and uncoupled currents during glutamate uptake by GLT-1 transporters. *J. Neurosci.* **22**, 10153–10162 (2002).
68. H. P. Larsson, A. V. Tzingounis, H. P. Koch, M. P. Kavanaugh, Fluorometric measurements of conformational changes in glutamate transporters. *Proc. Natl. Acad. Sci. U.S.A.* **101**, 3951–3956 (2004).
69. A. Auerbach, C. J. Lingle, Heterogeneous kinetic properties of acetylcholine receptor channels in *Xenopus myocytes*. *J. Physiol.* **378**, 119–140 (1986).
70. X. Zhuang *et al.*, Correlating structural dynamics and function in single ribozyme molecules. *Science* **296**, 1473–1476 (2002).
71. H. P. Lu, L. Xun, X. S. Xie, Single-molecule enzymatic dynamics. *Science* **282**, 1877–1882 (1998).
72. D. Min *et al.*, Unfolding of a ClC chloride transporter retains memory of its evolutionary history. *Nat. Chem. Biol.* **14**, 489–496 (2018).

73. T. K. Nayak, S. Dana, S. Raha, S. K. Sikdar, Activator-induced dynamic disorder and molecular memory in human two-pore domain hTREK1 K channel. *J. Chem. Biol.* **4**, 69–84 (2011).
74. Q. Xue, E. S. Yeung, Differences in the chemical reactivity of individual molecules of an enzyme. *Nature* **373**, 681–683 (1995).
75. F. Zosel, D. Mercadante, D. Nettels, B. Schuler, A proline switch explains kinetic heterogeneity in a coupled folding and binding reaction. *Nat. Commun.* **9**, 3332 (2018).
76. A. L. Blatz, K. L. Magleby, Correcting single channel data for missed events. *Biophys. J.* **49**, 967–980 (1986).
77. M. F. Juette *et al.*, Single-molecule imaging of non-equilibrium molecular ensembles on the millisecond timescale. *Nat. Methods* **13**, 341–344 (2016).
78. C. Joo, T. Ha, Preparing sample chambers for single-molecule FRET. *Cold Spring Harb. Protoc.* **2012**, 1104–1108 (2012).
79. C. E. Aitken, R. A. Marshall, J. D. Puglisi, An oxygen scavenging system for improvement of dye stability in single-molecule fluorescence experiments. *Biophys. J.* **94**, 1826–1835 (2008).
80. F. J. Sigworth, S. M. Sine, Data transformations for improved display and fitting of single-channel dwell time histograms. *Biophys. J.* **52**, 1047–1054 (1987).
81. C. Martens *et al.*, Direct protein-lipid interactions shape the conformational landscape of secondary transporters. *Nat. Commun.* **9**, 4151 (2018).
82. A. M. C. Lau, Z. Ahdash, C. Martens, A. Politis, Deuteros: Software for rapid analysis and visualization of data from differential hydrogen deuterium exchange-mass spectrometry. *Bioinformatics* **35**, 3171–3173 (2019).